Flow, Turbulence and Combustion manuscript No.
(will be inserted by the editor)

Implementation methods of wall functions in cell-vertex numerical solvers

Felix Jaegle · Olivier Cabrit · Simon Mendez · Thierry Poinsot

Received: date / Accepted: date

Abstract Two different implementation techniques of wall functions for cell-vertex based numerical methods are described and evaluated. The underlying wall model is based on the classical theory of the turbulent boundary layer. The present work focuses on the integration of this wall-model in a cell-vertex solver for large eddy simulations and its implications when applied to complex geometries, in particular domains with sudden expansions (more generally in presence of sharp edges). At corner nodes, the conjugation of law of the wall models using slip velocities on walls and of the cell-vertex approach leads to difficulties. Therefore, an alternative implementation of wall functions is introduced, which uses a no-slip condition at the wall. Both implementation methods are compared in a turbulent periodic channel flow, representing a typical validation case. The case of an injector for aero-engines is presented as an example for an industrial-scale application with a complex geometry.

F. Jaegle
CERFACS, 42 Av. Gaspard Coriolis, 31057 Toulouse Cedex 01, France
Tel.: +33-(0)5-61 19 31 09
Fax: +33-(0)5-61 19 30 00
E-mail: felix.jaegle@cerfacs.fr
present address:
Institute for aerodynamics and gas dynamics, University of Stuttgart, Pfaffenwaldring 21
D-70569 Stuttgart, Germany
E-mail: felix.jaegle@iag.uni-stuttgart.de

O. Cabrit
CERFACS, 42 Av. Gaspard Coriolis, 31057 Toulouse Cedex 01, France
E-mail: olivier.cabrit@cerfacs.fr

S. Mendez
CERFACS, 42 Av. Gaspard Coriolis, 31057 Toulouse Cedex 01, France
Present address:
Université Montpellier II, I3M UMR CNRS 5149, C.C. 051
Place Eugène Bataillon, 34095 Montpellier cedex 5, France
E-mail: smendez@math.univ-montp2.fr

T. Poinsot
Institut de mécanique des fluides de Toulouse (CNRS-INPT-UPS), Allée du Professeur-Camille-Soula, 31400 Toulouse, France
E-mail: thierry.poinsot@imft.fr

1 Introduction

A correct treatment of walls in Large Eddy Simulations (LES) of industrial-scale complex geometries remains a challenging task. Despite growing computing resources, mainly in the form of massively parallel machines, the resolution of boundary layer flows remains out of reach for routine application [19], making wall modeling a crucial ingredient of practical LES [13]. Alongside hybrid approaches of LES and RANS (Reynolds Averged Navier-Stokes) like Detached Eddy Simulation (DES [28, 27]), wall functions [4, 25] are often the method of choice for large LES cases (e.g. combustion chambers [24]). Here, wall functions avoid to resolve the turbulent eddies that are proportional in size to the wall-normal distance (as opposed to wall-resolved LES), as well as the strongest gradients in the viscous sublayer (which is still necessary when resolving RANS equations near the wall, as in DES approaches). The gain in terms of grid resolution is considerable [19], while very satisfying precision can be obtained even for complex flows [13].

The use of wall functions in LES was first published by Deardorff [4] in 1970 for a channel flow at infinite Reynolds number. This method was extended by Schumann [25] for a finite Reynolds number channel flow, but the method required the average wall shear stress to be known a priori. Grötzbach [6] modified Schumann's method for arbitrary channel flows but the wall shear stress was still evaluated for quantities averaged over the entire channel surface. Today's methods evaluate wall functions locally at each grid cell, following the approaches used by Mason and Callen [12] or Piomelli et al. [20]. A more detailed description of early applications of wall functions can be found in [20].

Wall-modeling for LES is often critically viewed because it combines models that are derived from ensemble-averaged equations for a turbulent boundary layer with an approach that is based on a spatial filtering argument. A common argument [19] is that, provided the first near-wall grid cell is large enough, it contains a sufficient number of turbulent structures (with typically faster turnover times than the outer flow) to justify the application of a wall model based on the ensemble-average of these structures in an unsteady LES. As Nicoud et al. [16] point out, this leads to a conflict of objectives in the mesh region directly above the first off-wall grid point. Here, the LES requires relatively isotropic grid cells that diminish in size towards the wall, whereas the wall model demands large grid cells for the statistical argument to hold. A typical mesh is therefore a compromise and generally leads to an under-resolved intermediate zone resulting in a loss of accuracy.

Building on the basic principle of the pioneering work, modern studies on wall function approaches mainly focus on the underlying wall-model. The goal is to take more physical phenomena into account, such as heat fluxes [6] or chemical reactions [3] to name some examples. This includes efforts to extend the validity of the wall-model to configurations including streamwise pressure gradients, wall-curvature or separated flows [8, 2], in which standard equilibrium formulations can be expected to perform poorly.

Another relevant subject is the interaction of the wall-model with the numerical scheme. While the pioneering papers on wall functions provide details on the actual

implementation method (an example is Schumann [25]), contemporary studies tend to give only superficial information on how the wall-model considered is implemented into a flow solver. This becomes even more critical for numerical methods that have a different structure than those used in the early studies [4, 25, 6]. In particular for less-widespread methods like cell-vertex based schemes, we are not aware of any study discussing implementation methods and their performance. Arguably, this lack of information is related to the use of the periodic channel flow as a standard test case for publications on wall-modeling, where the implementation method is indeed of little influence. In this paper, it will be shown that there are several ways to couple wall functions with a numerical scheme and that these differences can affect the results of a LES. Configurations like the flow over a corner reveal that classical implementation methods that perform soundly in the turbulent channel can be problematic in realistic applications. The study is limited to cell-vertex-type solvers.

The intent is to provide a guideline for implementation techniques aimed at the application on realistic configurations that often have complex geometries. The paper covers all elements that are relevant during the implementation process: in the first part, an example for a standard wall-model is presented, followed by a description of the cell-vertex formalism. In the next part, two methods methods to implement wall functions are detailed, together with their respective technical advantages and drawbacks. In the last part, both methods are evaluated in several test cases. First, they are compared in a turbulent channel flow, following a standard validation procedure. Then, the flow over a sudden expansion is considered as an example for a situation where one of the formulation encounters problems. Finally, the potential of a wall-modeling approach in realistic applications is demonstrated at the example of a premixing swirler for aero-engines.

2 Pre-requisites: wall-model and cell-vertex approach

2.1 Wall-model

Wall modeling in itself is not the main interest of the present work. Therefore, a very basic model using classical boundary layer theory is used and shall be presented briefly in the following. It should be noted that the implementation strategies presented in this paper can in principle be combined with other, more sophisticated wall law formulations. Furthermore, although turbulent heat transfer is an important part in a wall modeling approach, it shall be excluded in this paper, which will focus on momentum conservation.
The fully developed turbulent boundary layer flow over an infinite flat plate is considered. This implies that, in a Reynolds-averaged form, the problem is steady ($\partial/\partial t = 0$) and one-dimensional ($\partial/\partial x = 0$, $\partial/\partial z = 0$) with the wall-distance y being the only relevant spatial direction and the streamwise velocity $\overline{u}$ the sole non-zero mean velocity component. Here, Reynolds-averaged variables are denoted with the bar-operator $(\overline{\text{–}})$. The density ρ and the molecular dynamic viscosity μ are considered constant in this context. An additional assumption is the absence of chemical reactions. The momentum

equation of the time-averaged flow then reduces to:

$$\frac{\partial \overline{p}}{\partial x} = \frac{\partial \overline{\tau_{xy}}}{\partial y} - \frac{\partial}{\partial y} \underbrace{\overline{\rho}\,\overline{u'v'}}_{-\overline{\tau_t}} \tag{1}$$

Where $\tau_{xy} = \mu\ \partial u/\partial y$ is the viscous stress tensor and τ_t the Reynolds-stress tensor, which can be modeled using the Boussinesq assumption:

$$\tau_t = \mu_t \frac{\partial \overline{u}}{\partial y} \tag{2}$$

The case of a flat plate is characterized by the absence of a longitudinal pressure gradient $\partial \overline{p}/\partial x = 0$. The momentum equation written in terms of μ and μ_t then takes the following form:

$$\frac{\partial}{\partial y}\left(\frac{\partial \overline{u}}{\partial y}(\mu + \mu_t)\right) = 0 \tag{3}$$

This equation states that the total level of friction, $\tau_{tot} = \overline{\tau}_{xy} + \overline{\tau}_t$ is constant throughout the boundary layer. It implies that the total friction must be equal to the wall-friction, which corresponds to the viscous wall shear stress $\tau_w = \mu\ \partial\overline{u}/\partial y|_w$, since the turbulent stress vanishes at the wall due to the absence of any fluctuations. The subscript 'w' stands for variables evaluated at the wall. Integration of eq. 3 using $\tau_{tot} = \tau_w$ yields:

$$\frac{\partial \overline{u}}{\partial y}(\mu + \mu_t) = \tau_w \tag{4}$$

In boundary layer theory, it is convenient to introduce wall units, based on the friction velocity $u_\tau = \sqrt{\tau_w/\rho}$ and defined as:

$$y^+ = \frac{\rho u_\tau y}{\mu} \qquad u^+ = \frac{\overline{u}}{u_\tau} \tag{5}$$

In the inertial layer that is characterized by $\mu_t^+ >> \mu^+$, the Prandtl mixing length model [23] provides a closure for the turbulent viscosity. Integration of eq. 4 then yields the well-known logarithmic law:

$$u^+ = \frac{1}{k}\, ln(y^+) + C \tag{6}$$

where k is the Von Kármán constant [31]. The values commonly retained for the model constants are $k = 0.41$ and $C = 5.5$ for confined flows ($C = 5.2$ is rather preferred for external flows).

2.2 The cell-vertex approach

The *cell-vertex* approach is one of the common discretization methods for finite volume schemes, the very popular alternative being the *cell-centered* formulation [7, 30]. While in the latter case, flow variables are stored at the center of the cells, they are stored at the grid nodes in the former.
The key difference is the computation of fluxes through cell boundaries. For cell-centered schemes, the flux through a cell boundary is based on the reconstruction

from values at the centers of the neighbouring cells. In a cell-vertex scheme, the flux is obtained from the values at the nodes that delimit the cell boundary. The "vertices" are to be understood as points that coincide with the grid nodes but are associated to a grid cell. This means that one grid node can coincide with several vertices, one for each of the grid cells clustered around it.

Written in flux variables, the Navier-Stokes equations take the compact form

$$\frac{\partial \mathbf{U}}{\partial t} + \vec{\bigtriangledown} \cdot \vec{\mathcal{F}} = \mathbf{S} \tag{7}$$

where $\mathbf{U}$ is the vector of the conservative flow variables, $\vec{\mathcal{F}}$ the flux tensor of $\mathbf{U}$ and $\mathbf{S}$ the vector of source terms. The flux tensor can be decomposed in a convective part $\vec{\mathcal{F}}^C$ and a viscous part $\vec{\mathcal{F}}^V$:

$$\vec{\mathcal{F}} = \vec{\mathcal{F}}^C(\mathbf{U}) + \vec{\mathcal{F}}^V(\mathbf{U}, \vec{\bigtriangledown}\,\mathbf{U}) \tag{8}$$

The first important aspect of the *cell-vertex* method is the definition of metrics, in particular of the normal vectors. Here, S_f denotes the normal vector of a given element face (or edge in 2D), defined as pointing towards the exterior. Its length is weighted by the area of the element face (resp. edge length). The normal vector $\vec{S}_k$ at the vertex k of an element (pointing inward) is obtained by

$$\vec{S}_k = \sum_{f \ni k} -\frac{d}{n_v^f} \vec{S}_f \tag{9}$$

where d is the number of spatial dimensions and n_v^f the number of vertices of face f. Figure 1 illustrates the process of calculating $\vec{S}_{k_1}$, the normal at the vertex $k = k_1$ for a triangular and a quadrilateral element. It has to be noted that this method differs for domain boundaries as explained for diffusive fluxes at the end of this section.

Based on this element description, eq. 7 can be written in a semi-discretized form at node j:

$$\frac{d\mathbf{U}_j}{dt} = -\vec{\bigtriangledown} \cdot \vec{\mathcal{F}}^C\Big|_j - \vec{\bigtriangledown} \cdot \vec{\mathcal{F}}^V\Big|_j + \mathbf{S}\Big|_j \tag{10}$$

To obtain the divergence of the convective fluxes $\vec{\bigtriangledown} \cdot \vec{\mathcal{F}}^C\Big|_j$ the element residual R_e is calculated summing flux values located at all vertices k of the element e (the ensemble of these vertices being K_e):

$$\mathbf{R}_e = -\frac{1}{dV_e} \sum_{k \in K_e} \vec{\mathcal{F}}_k^C \cdot \vec{S}_k \tag{11}$$

Here, V_e is the element volume which is defined as (d being the number of spatial dimensions):

$$V_e = -\frac{1}{d^2} \sum_{k \in K_e} \vec{x_k} \cdot \vec{S}_k \tag{12}$$

The nodal value of the flux divergence is then obtained by summing the weighted residuals $V_e\,\mathbf{R}_e$ of all cells having a vertex coinciding with the node j (the ensemble of these cells being noted $\mathcal{D}_j$):

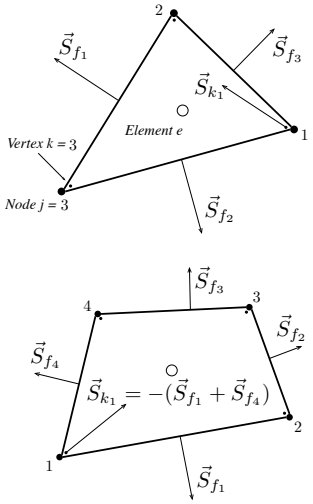

Fig. 1 Schematic of the face- (f) and vertex- (k) normals of a triangular and a quadrilateral element.

$$\vec{\nabla} \cdot \vec{\mathcal{F}}^C \Big|_j = \frac{1}{dV_j} \sum_{e \in \mathcal{D}_j} \underline{\mathbf{D}}_{j,e} V_e \, \mathbf{R}_e \tag{13}$$

This summation, called *scatter*-operation, is schematized in Fig. 2. The nodal volume $V_j = \sum_{e \in \mathcal{D}_j} V_e / n_v^e$ is called *dual cell* as it acts as a control volume during the residual *scatter*. Here, n_v^e is the number of vertices of an element e. The residual distribution matrix $\underline{\mathbf{D}}_{j,e}$ is a central part of the numerical scheme that is built upon the cell-vertex formalism and shall not be detailed here. Note that for the scheme to be conservative, the sum over all distribution matrices at the vertices of an element must be equal to unity [29]:

$$\sum_{k \in K_e} \underline{\mathbf{D}}_{k,e} = \underline{I} \tag{14}$$

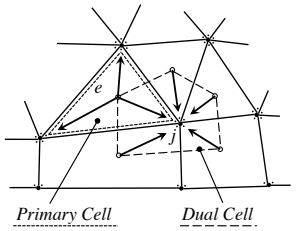

Fig. 2 Schematic of the cell-vertex formalism. The dotted line delimits an element e (primary cell), the dashed line the control volume of the node j (dual cell), arrows symbolize the scatter operation of an element residual to the surrounding nodes (eq. 13).

For the divergence of the viscous terms $\vec{\bigtriangledown} \cdot \vec{\mathcal{F}}^V$, the method applied differs from the one used for the convective fluxes. First, the gradient of the conservative variables $\left(\vec{\bigtriangledown} \mathbf{U}\right)_e$ is calculated for the element e. Using this gradient and the nodal value $\mathbf{U}_j$ allows to calculate the viscous flux tensor from element and node values:

$$\vec{\mathcal{F}}^V_{j,e} = \vec{\mathcal{F}}^V \left(\vec{\bigtriangledown} \mathbf{U}\right)_e \tag{15}$$

The divergence is then obtained by summing all contributions in the *dual cell* associated to the node j:

$$\vec{\bigtriangledown} \cdot \vec{\mathcal{F}}^V \Big|_j = \frac{1}{dV_j} \sum_{e \in \mathcal{D}_j} \vec{\mathcal{F}}^V_{j,e} \cdot \vec{S}_{j,e} \tag{16}$$

The normal vectors $\vec{S}_{j,e}$ used in this operation are located at the center of a given element e and associated to the node j. Figure 3 schematizes the location and direction of these normals. It can be shown that they are equal to the vertex normals $\vec{S}_k$, where the vertex k coincides with the node j considered.

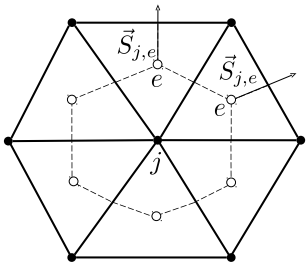

Fig. 3 Sketch of the normals $\vec{S}_{j,e}$ used for the diffusion scheme.

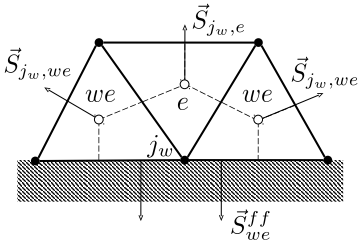

Fig. 4 Sketch of the face-based normals $\vec{S}^{ff}_{we}$ appearing at the application of Neumann boundary conditions on elements with boundary faces, noted we.

Applying Neumann boundary conditions in a finite volume framework corresponds to imposing fluxes through the domain boundary. To do this efficiently, the diffusive flux divergence operation in eq. 15 is modified for nodes located on wall boundaries,

noted j_w (see Fig. 4): the prediction of the diffusion scheme is corrected by adding fluxes given by the boundary condition, $\vec{\mathcal{F}}^{BC}_{j_w,we}$.

$$\vec{\bigtriangledown} \cdot \vec{\mathcal{F}}^V \Big|_{j_w} = \underbrace{\frac{1}{dV_{j_w}} \sum_{e \in \mathcal{D}_{j_w}} \vec{\mathcal{F}}^V_{j_w,e} \cdot \vec{S}_{j_w,e}}_{\text{Diffusion scheme prediction}} + \underbrace{\sum_{we \in \mathcal{D}_{j_w}} \vec{\mathcal{F}}^{BC}_{j_w,we} \cdot \vec{S}^{ff}_{we}}_{\text{Boundary correction}} \tag{17}$$

Instead of $\vec{S}_{j,e}$, the correction term uses face-based normal vectors, noted $\vec{S}^{ff}_{we}$. They are defined as the normals of an element face located on the boundary, as shown in Fig. 4 for the boundary elements (denoted by we). Equation 17 clearly shows that Neumann boundary conditions only have a direct effect on the grid nodes located at the domain boundary (jw). This also means that Dirichlet boundary conditions cannot be applied simultaneously, because they would affect the same nodes (jw) and thus effectively overwrite the flux corrections. It should be noted that in a cell-centered framework, this limitation does not exist, as fluxes do not appear at the same location as the flow variables.

2.3 The use of wall functions in LES solvers

In sections 2.1 and 2.2, the wall model and the numerical framework have been described. The missing ingredient for the implementation of wall laws is how numerics and wall model are combined *in a LES context*. For the sake of clarity, the following paragraphs are limited to a one-dimensional view (in wall-normal direction), analogous to turbulent boundary layer theory. The shear balance in the element adjacent to the wall (noted 'we') takes the form:

$$\tau_{xy}\Big|_{we} = \frac{d\,\hat{u}}{dy}\Big|_{we} (\mu + \mu_{sgs}|_{we}) = \frac{\hat{u}_2 - \hat{u}_1}{\Delta y} (\mu + \mu_{sgs}|_{we}) \tag{18}$$

where u_1 and u_2 are the velocities at directly on the wall and on the first grid point respectively, '$\hat{}$' is the LES filter operator, Δy is the wall-distance of the first point and μ_{sgs} the subgrid-scale viscosity. In cases of low near-wall grid resolution, this equation cannot yield correct results: the subgrid-scale viscosity is given by a LES model that is designed to account for stresses in the unresolved scales of turbulence. Near the wall, however, typical models will fail to predict the wall shear stress correctly, as they are not based on physical arguments related to under-resolved, wall-bounded flows. Instead, their behaviour is known to be often unphysical in under-resolved boundary-layers or generally in zones of pure shear [15], for instance in the case of the Smagorinsky model [26].

The central idea of wall functions consists in locally using boundary layer theory (of the type layed out in section 2.1) in lieu of the diffusion scheme to restore the correct balance in eq. 18. In the element adjacent to the wall, the predicted shear stress $\tau_{xy}|_{we}$ is corrected by a value obtained from a wall model, $\overline{\tau}^{model}_w$.

$$\tau_{xy}\Big|_{we} = \overline{\tau}_w^{model} \tag{19}$$

In the present study, $\overline{\tau}_w^{model}$ is obtained from the logarithmic law (eq. 6). Written in flow variables, it reveals its practical property of relating the wall shear stress to any point in the velocity profile located inside the inertial layer:

$$\hat{u} = \frac{1}{k}\sqrt{\frac{\overline{\tau}_w}{\rho}}\, ln\left(\frac{\rho y\sqrt{\overline{\tau}_w/\rho}}{\mu}\right) + C \tag{20}$$

In practice, this equation can be resolved numerically or interpolated from lookup tables to provide the wall shear stress as a function of the velocity $\hat{u}_2$ at the first off-wall point with the wall distance Δy (assuming ρ_{we} and μ_{we} to be constant):

$$\overline{\tau}_w = f(\Delta y, \hat{u}_2) \tag{21}$$

Note that this approach involves Reynolds-averaged variables (noted with the bar operator ‘ $-$ ’) as filtered variables of the LES. In a wall function approach, it is generally assumed that the near-wall control volume contains a sufficient number of turbulent structures for a Reynolds averaged view to be justified, even in an instantaneous flow field [19]. RANS quantities in the first cell can therefore be combined with instantaneous variables of the LES.

The following sections describe in detail different options of applying eq. 20 to the numerical scheme as a wall boundary condition.

3 Implementation methods

3.1 Implementation as a wall-boundary condition

The first method to be discussed is considered the standard for cell-vertex solvers because it is straightforward to implement and is therefore widely used in literature [16, 24, 17, 11, 13]. It starts from the idea that the wall-function should be applied through a conventional boundary condition, i.e. the locations where values are imposed should be limited to the nodes on the domain boundary (see eq. 17). In view of the cell-vertex formalism, this means that the physically motivated no-slip condition at the wall nodes has to be replaced by a no-transpiration condition if a wall-normal shear stress is to be prescribed there.
In practice, the procedure is as follows: the scheme calculates a momentum flux (the wall-normal component being τ_{xy}) at the cell-center we. These predictions are scattered to all surrounding nodes. The values of τ_{xy} that are sent to a wall-node jw are then replaced by the value given by the wall-function τ_w (eq. 17, illustrated in Fig. 5). In an arbitrary 3D geometry, this correction is applied selectively on the wall-normal component of the momentum flux, the direction of shear being aligned with the wall-parallel velocity vector. The wall-normal velocity is set to zero ($u_{1,\perp} = 0$) as a Dirichlet-type boundary condition (classical Dirichlet or the NSCBC (for Navier Stokes Characteristic Boundary Conditions) [22] equivalent). As the no-slip condition on the wall-parallel velocity had to be removed, this method generally leads to a slip-velocity appearing on the wall, as illustrated in Fig. 6. Most studies that provide information

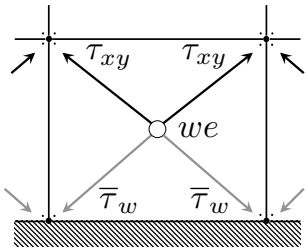

Fig. 5 Application of the wall functions in the slip-wall formulation. Schematic of the *scatter* operation of the momentum flux contributions. Black arrows correspond to contributions calculated by the diffusion scheme, grey arrows to contributions corrected by the wall function.

on implementation methods justify this slip velocity as a point on the velocity profile at the wall-distance δ. An example is the study of Panara et al. [17] (Fig. 7 a) where it is assumed that the slip velocity is $0 < u_1 < u_2$, which means that there is a point on the theoretical profile with $u(y = \delta) = u_1$. It is further assumed that δ can be neglected and that therefore u_1 is a valid approximation of the theoretical profile. Another example is Mohammadi et al. [13], who assume that the computational domain ends at a wall-distance δ that is large enough to reach into the log-layer (see Fig. 7 b). The slip velocity is then equivalent to the velocity in the log-layer u_2.

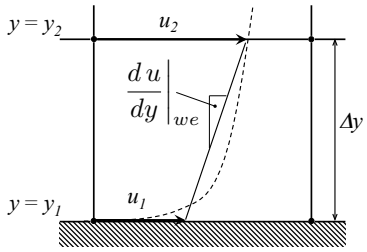

Fig. 6 Overview of the most important variables appearing in the formulation with a slip velocity.

3.2 Implementation without slip velocity at the wall

In certain cases, it can be preferrable to avoid a slip-velocity at the wall as will be discussed in detail in section 3.4. The central requirement for an alternative implementation method is therefore that the physically motivated no-slip condition can be imposed at the wall nodes. By doing so, however, one makes it impossible to apply the corrected wall shear stress at the same location. This is because, in a given time step,

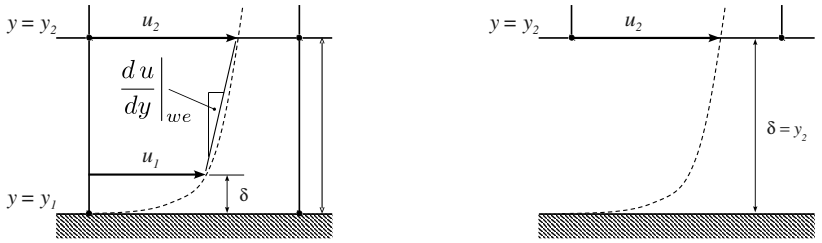

a) b)

Fig. 7 Alternative interpretations of the slip-wall function approach.

the corrected contributions of the diffusion scheme τ_{we} exclusively affect the nodes they are directed to. Neighbouring nodes are only influenced indirectly in subsequent time steps. A Dirichlet-condition, imposed after the computation of the diffusive terms will therefore cancel out any effect of the numerical scheme on these nodes. The logical alternative is to apply the wall function away from the wall, at the upper nodes of the first cell, as shown in Fig. 8. This choice is in fact consistent with the underlying boundary layer theory, as eq. 3 clearly shows that the shear is constant throughout the first wall cell (equal to τ_w). The fact that the gradient inside the wall element (Fig. 9) is unphysically high has no consequence in this case, because the diffusion scheme is inactive in this cell, its predictions being replaced by the wall function and the no-slip condition.

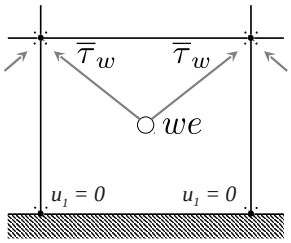

Fig. 8 Application of the wall functions in the no-slip formulation. Schematic of the *scatter* operation of the momentum flux contributions. Grey arrows symbolize the contributions corrected by the wall function.

An overview of the key differences between both implementation methods can be obtained from table 1, where a simplified sequence of events during a numerical time step is presented.

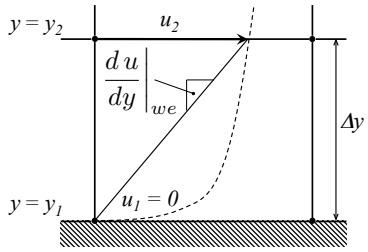

Fig. 9 Overview of the most important variables appearing in the no-slip formulation.

No-slip wall law	**Slip wall law**
Initial field of conservative variables $\mathbf{U}$	
Calculation of the flux tensor $\vec{\mathcal{F}}$	
Neumann boundary conditions	
τ_w at y_2 (1st off-wall node)	τ_w at y_1 (wall)
Advancement in time: $\partial\mathbf{U}/\partial t + \vec{\bigtriangledown} \cdot \vec{\mathcal{F}} = \mathbf{S}$	
New field of conservative variables $\mathbf{U}$	
Correction of conservative variables $\mathbf{U}$ Dirichlet boundary conditions	
$u_1 = 0$	$u_{1,\perp} = 0$
Final field of conservative variables $\mathbf{U}$	

Table 1 Comparative overview of the no-slip and slip wall function implementations. Simplified sequence of events during one computational time step.

3.3 Alternative implementation methods in literature

The list of implementation methods discussed up to this point is not exhaustive - methods may vary in detail but there are also entirely different strategies. One example is the work of Breuer et al. [2] who use the subgrid-scale viscosity to apply the information given by the logarithmic law (eq. 20) into a solver. In principle, any value in the near-wall shear balance (eq. 18) can be corrected to impose the wall-shear stress.
In cell-vertex codes, however, the SGS-viscosity is subject to gather and scatter operations as it is calculated at the cell center and then stored at the nodes. This means that some smoothing is always introduced and it may be difficult (depending on how a code is structured) to impose exact values at a precise location in the near-wall cell. It is therefore often preferred to correct the wall-normal momentum fluxes as they correspond directly to the wall-normal stresses.

In the following, the discussion will be limited to two implementation methods: the first is the standard procedure as illustrated in fig. 6 and will be referred to as the slip-wall formulation. The second is the alternative method based on a no-slip condition that will be referred to as the no-slip formulation.

3.4 Critique of the implementation methods

Although there are various ways to justify the slip velocity that cannot be avoided if the wall-shear stress is applied as a boundary condition, the practical use of the slip-wall formulation should proceed with caution. For the variant shown in Fig. 7 a), the slip velocity must satisfy $0 < u_1 < u_2$ in order to have a sensible physical interpretation. The main limitation is that the magnitude of the slip velocity u_1 depends predominantly on the level of subgrid-scale viscosity in the wall element. This becomes clear when rearranging eq. 18 at the wall-element with $\overline{\tau}_w$ obtained from the wall function:

$$\left.\frac{d\,\hat{u}}{dy}\right|_{we} = \frac{\overline{\tau}_w(\hat{u}_2, y_2)}{\mu + \mu_{sgs}|_{we}} \tag{22}$$

Assuming that the velocity at the first node above the wall behaves ideally and thus coincides with the log-law for a given $\overline{\tau}_w$ and the molecular viscosity μ is constant, this equation yields a gradient that will establish between y_1 and y_2, which depends only on μ_{sgs} (see Fig. 6 for an illustration). This relation reveals that the method is well-suited for the use in conjunction with the Smagorinsky model, for which μ_{sgs} does not vanish near the wall, leading to raised levels of subgrid-scale viscosity and thus to a moderate gradient. In contrast, when used with turbulence models that yield near-zero subgrid-scale velocity at the wall (e.g. the WALE model [15]), this gradient will be very steep and could potentially lead to reversed slip-velocities ($u_1 < 0$), causing spurious oscillations.

To provide a certain estimate for the domain of validity of the slip-wall formulation, a relation for the magnitude of u_1 is developed at the example of the Smagorinsky model. In a time-averaged ($\langle\rangle$-operator), one-dimensional form (assuming a linear discretization of the velocity profile), the expression for $\mu_{sgs}|_{we}$ reads:

$$\langle \mu_{sgs}|_{we} \rangle = \langle \rho \rangle \, (C_s \Delta)^2 \, \frac{(\langle \hat{u}_2 \rangle - \langle \hat{u}_1 \rangle)}{y_2} \tag{23}$$

Here, C_s is the Smagorinsky constant and Δ a length scale for the cell size. The slip-velocity can be estimated as:

$$\langle \hat{u}_1 \rangle = \langle \hat{u}_2 \rangle - y_2 \, \frac{\langle \overline{\tau}_w \rangle}{\langle \mu \rangle + \langle \mu_{sgs}|_{we} \rangle} \tag{24}$$

Combining equations 23 and 24 finally allows to obtain the average slip velocity $\langle \hat{u}_1 \rangle$ explicitely:

$$\langle \hat{u}_1 \rangle = \langle \hat{u}_2 \rangle - \frac{y_2}{2\,\langle \rho \rangle (C_s \Delta)^2} \left(-\langle \mu \rangle + \sqrt{\langle \mu \rangle^2 + 4 \langle \rho \rangle (C_s \Delta)^2 \langle \overline{\tau}_w \rangle} \right) \tag{25}$$

An evaluation of eq. 25 over a wide range of parameters shows that u_1 takes values that are roughly contained in an interval of $u_2 > u_1 > 0.75\,u_2$, indicating that for most

applications using the Smagorinsky model, the slip-velocity is indeed positive (and thus physical in the sense of Fig. 7 a)).

Any procedure that allows a slip-velicity at the wall will lead to a difficulty at corner points. Unlike the Neumann boundary conditions that are applied on the boundary face (see equation 17), the Dirichlet conditions of zero wall-normal velocity are applied directly on the conservative variables at the nodes. At the node coinciding with the corner, the definition of the wall-normal vectors is ambiguous (see Fig. 10). Following the standard procedure of calculating the nodal wall normal $\vec{S}_j^b$ as the average of the surrounding boundary-face normals $\vec{S}_e^{ff}$, the resulting normal at the corner point $\vec{S}_{j,c}^b$ (and consequently also the velocity vector) would take an unphysical angle of ≈ 45 degrees. Therefore, at the corner point only, the normal is either chosen equal to the one of the upstream boundary face or set to zero (removing all constraints on the direction of the velocity). Both methods lead to a nodal velocity vector that is aligned with the upstream wall. As a result, however, mass conservation will no longer be respected because of a flux through the boundary face situated at the downstream wall, as illustrated in Fig. 11.1. To correct that, a (face-based) Neumann boundary condition of zero mass flux can be applied instead of the Dirichlet condition of zero normal velocity. This ensures mass conservation but the correction of the face downstream of the corner effectively reduces the slip-velocity at the corner, leading to perturbations of the flow-field in this area. As the wall-element in a mesh adapted for wall functions is of a relatively large size in order to reach into the inertial layer, these perturbations can take magnitudes that lead to unphysical flow fields or numerical instabilities (see section 4.2).

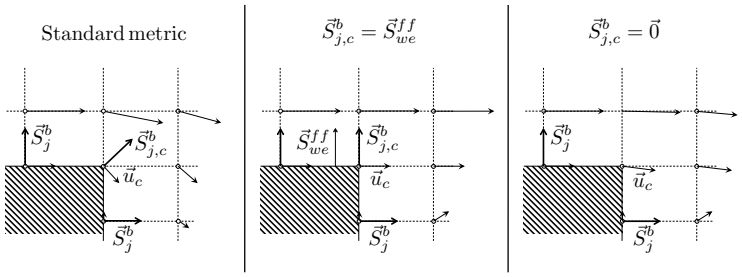

Fig. 10 Schematic illustration of different definitions of the nodal normal vector $\vec{S}_{j,c}$ at the corner node. Generic configuration of a flow over a corner.

Note that these difficulties are limited to the cell-vertex approach, as illustrated in Fig. 11: for a cell-centered formulation (Fig. 11.3), the wall-normal vector ambiguities and problems of mass-conservation do not appear due to the location of the velocity vectors at the cell-center. In a cell-vertex formalism, these problems can easily be overcome if a no-slip condition is imposed at the wall nodes as shown in Fig. 11.2. The following sections are therefore dedicated to wall functions with a no-slip condition at the wall.

The no-slip formulation removes all difficulties related to domains with corners. However, it adds some difficulty to the implementation for certain near-wall element

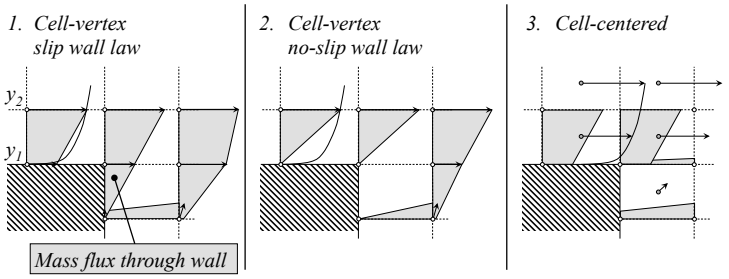

Fig. 11 Schematic of mass fluxes in vicinity of a corner ('→' symbolizes a momentum vector), comparing a cell-vertex scheme with/without slip velocity to the cell-centered approach. Generic configuration of a flow over a corner.

types. The slip-wall formulation can be deployed on any type of mesh, as it is an approach limited to the boundary of the domain. The no-slip approach, as it acts inside the fluid *volume*, is more sensitive to grid topology. The key example is a pure tetraedra mesh (Fig. 12 a), where the algorithms to establish the connectivity to the off-wall vertices (where the wall function would be applied) are complex and costly. Furthermore, the irregular wall-distances (for example the variation marked Δy_{23} in Fig. 12 a) have led to oscillatory behaviour in the tests that were conducted. The no-slip approach is therefore better suited for all sorts of prismatic elements (typically prisms and hexaedra, see Fig. 12 b) that ensure uniform wall-distance and straightforward access (in terms of connectivity) to the 'upper' element vertices. The capability of treating hybrid, unstructured meshes is therefore considered as a prerequisite for the use of no-slip wall functions in complex geometries. This is not a very strong limitation as the use of prismatic elements near the wall can generally be expected to lead to better results than a purely tetrahedral mesh.

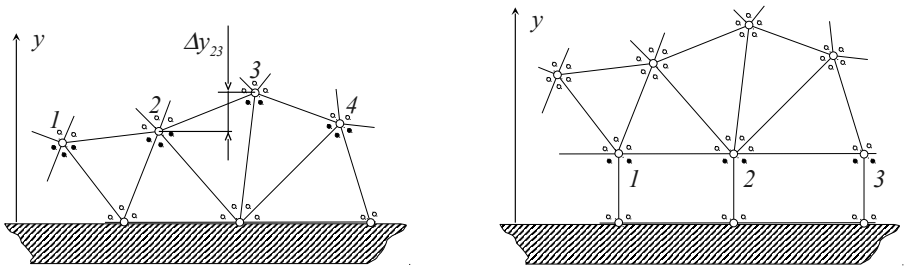

a) b)

Fig. 12 Implementation in a triangular (tetrahedral in 3D) mesh (a) and a hybrid mesh (b). The vertices represented as closed symbols are the locations where flux corrections are applied in the no-slip formulation.

#	Re_b	Re_τ	y^+	grid nodes (n_x,n_y,n_z)	$2\,\delta$ $[m]$
1	20 000	≈ 322	≈ 30	29 x 21 x 29	$1.5\ 10^{-3}$
2	40 000	≈ 594	≈ 50	33 x 25 x 33	$3.0\ 10^{-3}$
3	80 000	≈ 1100	≈ 100	25 x 23 x 25	$6.0\ 10^{-3}$
4	200 000	≈ 2524	≈ 100	33 x 51 x 33	$1.5\ 10^{-2}$
5	400 000	≈ 4798	≈ 150	33 x 61 x 33	$3.0\ 10^{-2}$
6	2 000 0000	≈ 20816	≈ 1000	41 x 41 x 41	$1.5\ 10^{-1}$

Table 2 Summary of the turbulent periodic channel cases.

4 Applications and Results

In the following, three application cases are presented. The first is a turbulent channel flow that serves as a basic validation case. The second is the flow over a sudden expansion that illustrates the implications of the corner problem described in 3.4. The third is a an aeronautical injector as an example for a complex, industrial-scale geometry.

4.1 Turbulent channel flow

A Large Eddy Simulation of a periodic channel flow is the most simple configuration with solid boundaries for which reference data in the form of analytical solutions as well as data from direct simulations are available. It should be noted that the purpose of this section is to present a typical procedure that is used to *validate* a new implementation, and to provide the reader with a general idea of the results that can be achieved with a standard wall-modeling approach and highlight certain effects of the different implementation methods. Due to the coarse near-wall grid resolution that is typical for any wall function approach, results are always affected by several sources of error that are not or only indirectly related to the wall treatment. A detailed assessment of the accuracy of wall-function approaches is therefore not in the scope of this work.
The configuration consists of a doubly periodic box (in x- and z direction) with walls on the top and bottom surfaces (in y-direction). Six different cases are considered (a summary is given in table 2), distinguished by different Reynolds numbers, such as Re_b (based on bulk properties, subscript 'b') and the friction Reynolds number Re_τ, defined as:

$$Re_b = \frac{\rho D_h\, u_b}{\mu} \qquad Re_\tau = \frac{\rho\, \delta\, u_\tau}{\mu} \tag{26}$$

Where $D_h = 4\delta$ is the hydraulic diameter and δ the channel half-width. The box size varies between $Lx+ = 1,290$; $Ly+ = 643$; $Lz+ = 643$ (for case #1) and $Lx+ = 80,000$; $Ly+ = 40,000$; $Lz+ = 40,000$ (for case #6). The mesh in all cases is of uniform, cartesian type with grid resolutions adapted to the respective values of Re_b. The grid cells are approximately isotropic in spanwise direction, with $\Delta z \approx \Delta y$ (depending on the case) and slightly anisotropic ($\Delta x \approx 2\Delta y$) in streamwise direction. All results are obtained using the second-order accurate Lax-Wendroff scheme [14] and a standard Smagorinsky formulation [26] for the subgrid-scale turbulent viscosity.

Statistics are presented in Fig.s 13 and 14 for a single, typical case (# 4) at $Re_b = 200\,000$, which corresponds to a friction Reynolds number of $Re_\tau \approx 2524$.

Figure 13 shows profiles of dimensionless longitudinal velocity u^+. There is a good agreement between the logarithmic law, DNS data of Hoyas and Jiménez [9] and both LES simulation results near the first grid point, showing that the most direct effect that wall functions have on the flow is correctly reproduced. In the region of the first few grid points towards the center of the channel, profiles from both wall functions start to deviate from the logarithmic law, an effect that is slightly stronger in the no-slip formulation. This is due to various sources of error related to the numerical sheme or the turbulence model. Another well-known effect is related to under-resolved and thus unphysical turbulent mechanisms near the wall, which are a result of the inherent lack of grid resolution that is described, for instance, by Nicoud et al. [16] (in the context of a wall function approach) and studied in a more general context by Piomelli et al. [21]. In this intermediate layer, the subgrid-scale viscosity is given by a LES model and therefore takes values that are lower than a turbulence model in a RANS approach would predict, leaving a share of the stress balance to be accounted for by resolved Reynolds stresses. On the other hand, the grid resolution in these zones is determined by the wall function approach and therefore too coarse to resolve turbulent structures at scales small enough for a LES to result in correct Reynolds stresses. A study of the resolution requirements in LES of shear flows can be found in the work of Baggett et al. [1]. Differences between both formulations can be observed on the velocity fluctua-

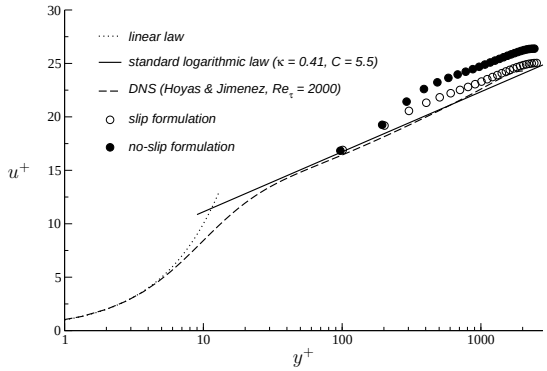

Fig. 13 Turbulent channel, dimensionless velocity profiles for case #4 ($Re_\tau \approx 2524$). Comparison between the analytical profile, DNS data [9] and LES results, obtained with a second-order Lax-Wendroff scheme, using wall functions in slip- and no-slip formulation. Case of $Re_b = 200000$.

tion profiles shown in Fig. 14 where the peak of the no-slip wall functions is displaced by approximately one point away from the wall with respect to the one of the slip-wall function. This indicates that for the slip-formulation the under-resolved near-wall vortical structures can be accomodated by the wall nodes thanks to the presence of a slip velocity, whereas in the case of the no-slip results, these structures are shifted away from the wall (Fig. 15), which seems to slightly increase their negative effect.

An overview of the global performance of both wall functions over a wide range of Reynolds numbers is shown in Fig. 16. Here, the mean friction coefficient C_f of the channel flow is compared to the classical correlations of Kármán and Nikuradse [10] as well as Petukhov [18]. The general trend observed is that for low Reynolds numbers, the slip-formulation yields superior results but deteriorates slightly for increasing Re_b.

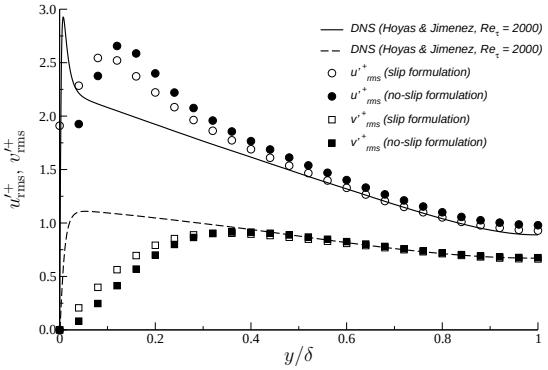

Fig. 14 Turbulent channel, dimensionless velocity fluctuation profiles for case #4 ($Re_\tau \approx 2524$). Comparison between the analytical profile, DNS data [9] and LES results, obtained with a second-order Lax-Wendroff scheme, using wall functions in slip- and no-slip formulation. Case of $Re_b = 200000$.

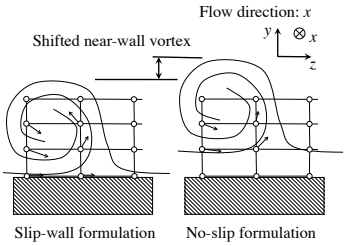

Fig. 15 Sketch of the effect of shifted near-wall vortical structures comparing slip- and no-slip formulations.

Inversely, the no-slip formulation shows the largest errors for low Reynolds numbers with increasingly good agreement for growing Re_b, eventually surpassing the accuracy of the slip-formulation. This observation can be explained by the diminishing influence of the near-wall effects relative to the channel height that work to the disadvantage of the no-slip formulation.

As applications with complex geometries such as the one presented in section 4.3 often use tetrahedral meshes, an additional simulation using hexahedral elements has been conducted. It is based on parameters identical to case #4 (table 2), including grid spacing, and uses the slip-wall formulation. The result shows slightly different friction levels but the error on C_f is comparable to case #4 using a hexahedral mesh.

4.2 Illustration of the corner problem: the flow over a sudden expansion

The turbulent channel flow of section 4.1 revealed only minor differences between implementation methods. Based uniquely on this test-case and considering its ease of implementation, the classical slip-wall formulation must appear as the preferrable method. On the other hand, in more complex geometries that feature sharp edges, the corner problem becomes a major limitation of the slip-wall formulation while at the same

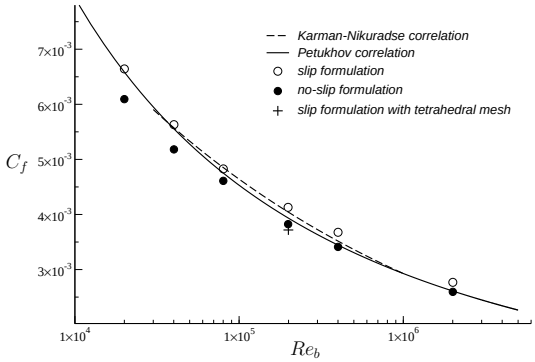

Fig. 16 Wall friction coefficient C_f as a function of the Reynolds number Re_b based on the bulk velocity in the channel. Comparison of slip- and no-slip results with correlations of Kármán and Nikuradse [10] as well as Petukhov [18].

time, it can be expected not to affect the no-slip formulation. To illustrate this advantage, the flow over a sudden expansion is considered (see Fig. 17). The example shown here follows the lines of the experiment of Dellenback et al. [5] at a Reynolds number of 30 000. The mesh is composed entirely of hexahedral elements with 10 cells across the diameter of the upstream tube, which results in a first off-wall grid point situated at approximately 160 wall units. This geometry, in conjunction with the rather coarse

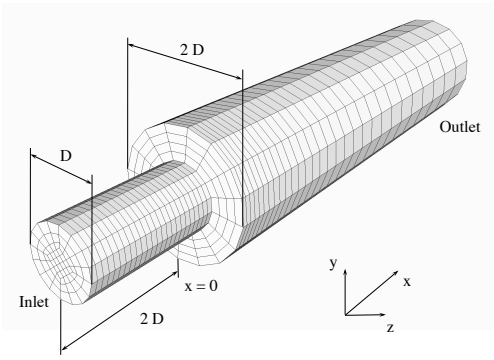

Fig. 17 Flow over a sudden expansion: Mesh and geometry overview.

grid resolution, is typical for certain geometrical details in very large LES cases, which often include small-scale jets that are emitted by tubes or ducts into a larger reservoir. Examples are dilution holes, injection points for gaseous fuel in combustion chambers or the narrow passage around the valves of an internal combustion engine, which are often meshed quite coarsely. It is typically this kind of configuration where the corner problem leads to undesired numerical artefacts.

Qualitative differences between the wall-law formulations can be observed on the iso-contours of mean axial velocity shown in Fig. 18. The flow field remains totally

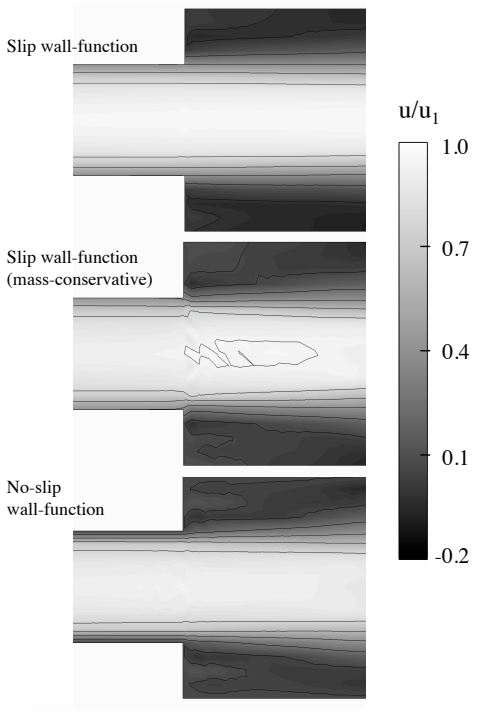

Fig. 18 Mean axial velocity iso-contours of the flow over a sudden expansion. Top: slip wall function without correction (not mass-conservative). Center: slip wall function with correction. Bottom: no-slip wall function.

unaffected (Fig. 18, top) for slip wall functions in their non-conservative form, i.e. without correction of wall-normal mass flux (see section 3.4, Fig. 11). However, the absence of this correction leads to an unphysical mass flux through the wall downstream of the step that amounts to approximately 15 % of the global mass flux. On the other hand, when the mass-flux correction is applied (Fig. 18, center), a notable perturbation of the flow field can be observed at the corner points and causes numerical oscillations over the entire diameter. These oscillations are not observed for wall functions in the no-slip formulation (Fig. 18, bottom), which is mass-conservative and shows a smooth, unperturbed flow field at the same time.

4.3 Injector for aero-engines

The last application is an idealized laboratory combustion chamber with one single premixing swirler like it is typically found in the latest generation of aero-engine combustors (Fig. 19). It is an example for one of the more complex geometries encountered in LES. The swirler is characterized by three stages, each composed of a series of narrow channels separated by the guide vanes, as highlighted in the right part of Fig. 19. Here,

it is operated in a purely aerodynamic regime (without liquid fuel injection or combustion) in order to assess the influence of the wall-model implementation method. The chamber is pressurized at 4.3 bar, the air fed into the plenum is pre-heated to 473 K, which corresponds roughly to the operating conditions of an engine at partial load. A bulk Reynolds number of the outer swirler channels is approximately $25,000$. A bulk Reynolds number of the chamber (based purely on global mass flux and cross-section) is approx. $120,000$. The airflow from the plenum to the chamber is split between the three-staged swirler and a cooling film placed near the circumference of the chamber upstream wall.

Owing to the complexity of the computational domain, the grid is composed of tetra-

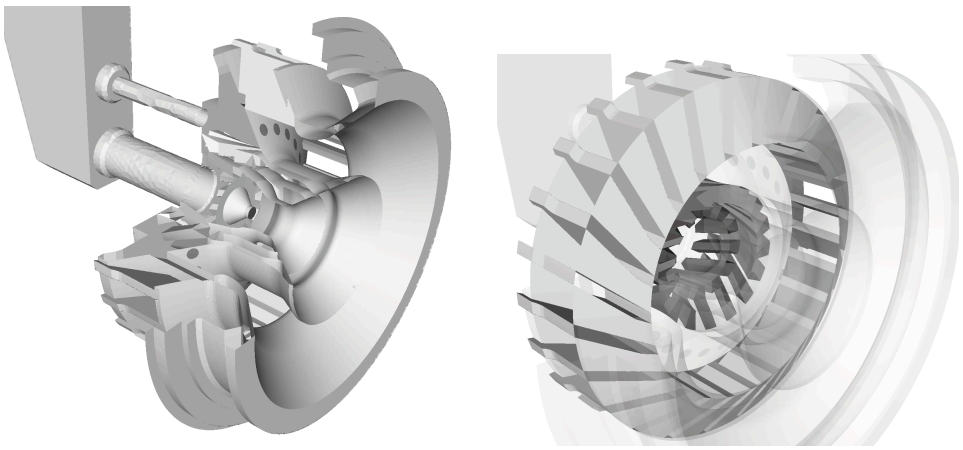

Fig. 19 Left: cut-away view of the injector. Right: transparent view with swirler stages highlighted.

hedral elements in its volume and of one single layer of prismatic elements at the boundary where wall functions are applied (see section 3.4 for details on the necessity of this method). This approach is applicable in arbitrary geometries as it simply consists in extruding the triangular tesselation of the domain boundary towards the inside. However, the more prismatic layers one chooses to apply or the thicker the layers are, the more the prisms tend to be distorted on sharp edges or corners. A view of the mesh and a detail of the prismatic layer is shown in Fig. 20. The thickness of the prism layer is varied locally and carefully adapted to be as close to 100 wall units. A visualization of instantaneous values of y^+ is given in Fig. 21. The resulting mesh comprises approximately 8.5 million cells and 1.6 million nodes. The simulations were performed using the second-order accurate Lax-Wendroff scheme [14] and a standard Smagorinsky formulation [26] for subgrid-scale turbulent viscosity. In the two simulations compared below, the only difference is the wall treatment. Everything else remains the same (mesh, algorithms, time step).

Quantitative results are presented in the form of mean velocity profiles (Fig. 23) and RMS velocity profiles (Fig. 24). In both figures, the axial and tangential components obtained with both wall function formulations are compared to experimental data provided by ONERA Fauga-Mauzac. The profiles are extracted over three transverse lines positionned at 10, 15 and 30 mm downstream of the swirler exit (see figure 22). The

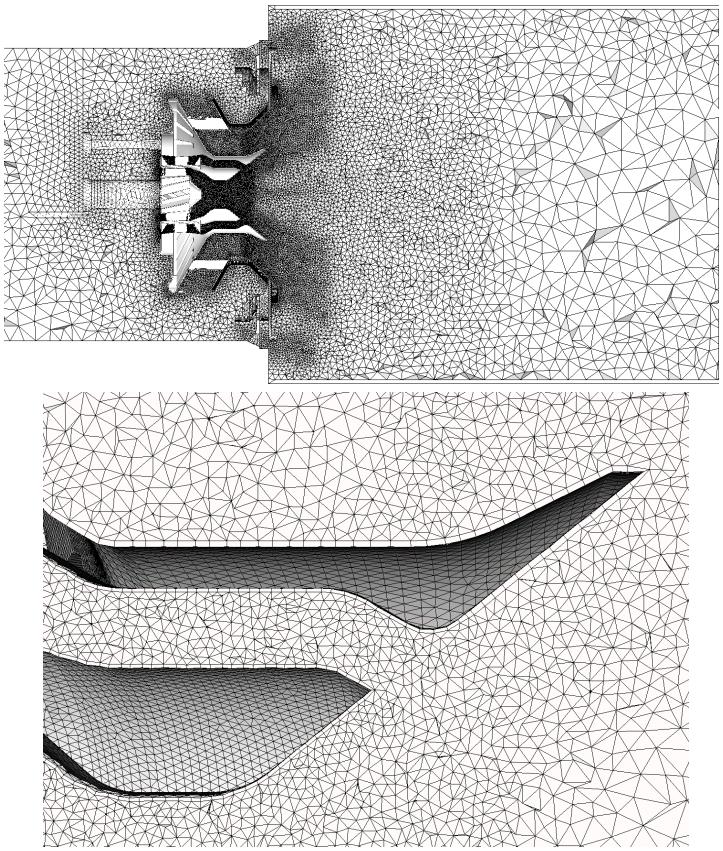

Fig. 20 Mesh overview and detail of hybrid wall boundary region with a layer of prismatic elements.

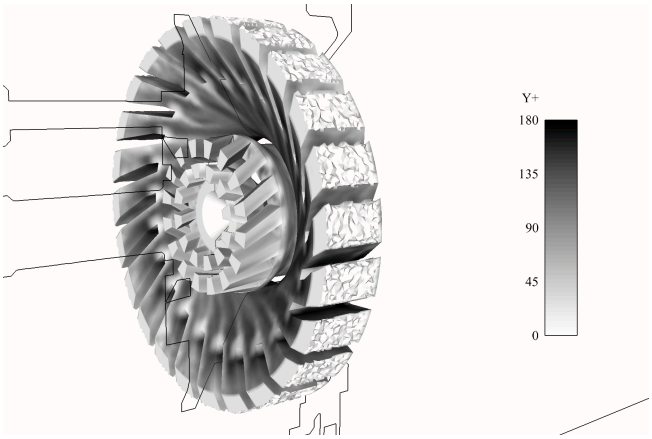

Fig. 21 Distance in wall units of the first off-wall grid point (y^+) for the instantaneous flow field (result obtained with the no-slip formulation).

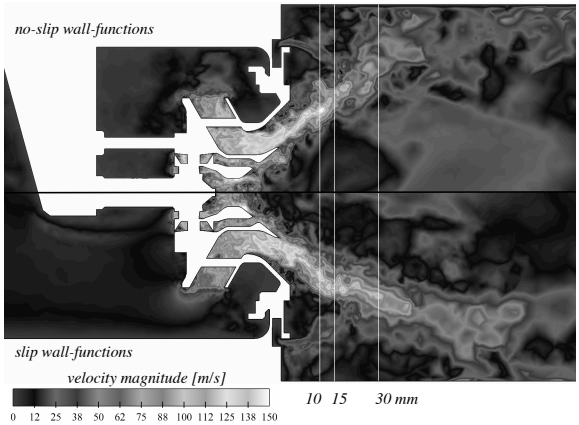

Fig. 22 Instantaneous velocity magnitude contours on a central cross-section through the domain. Upper half: result obtained using no-slip wall functions. Lower half: result obtained using slip wall function. White lines: positions of the extraction of velocity profiles.

agreement of the no-slip results in axial direction with experimental data is excellent, both the position and the magnitude of the peaks corresponding to the central flow and the cooling films are accurately reproduced. This is observed on all three measurement positions. The results of the slip wall functions are less satisfying because the peaks of the main flow are shifted slightly towards the center, indicating that the opening angle of the cone-shaped flow is too small. Purely qualitatively, this discrepancy in opening angle can also be observed on the instantaneous velocity field, shown in figure 22. As a consequence, the peak magnitudes increase, a behavior that is observed consistently at all three positions. In the tangential direction, the same observations can be made: very good agreement for the no-slip formulation and an over-estimation of tangential velocity peaks due to a under-estimated opening of the main flow.

Differences are less pronounced for the axial velocity fluctuations shown in figure 24. Here, the magnitude of the strongest fluctuations in the turbulent shear layer between the main flow and the central recirculation zone is well captured in both simulations. Differences are observed on the third measurement line at 30 mm, where the offset of the peaks from the slip wall function results becomes most noticeable. In tangential direction, fluctuations are slightly over-estimated on the first measurement line (10 mm) in both simulations. Downstream, the agreement is better for the no-slip results, while the slip wall functions again show over-estimated peaks displaced towards the inside.

The quality of both LES (without considering the differences resulting from wall modeling) is very satisfying as shown by the results obtained using the no-slip wall function approach. With all other simulation parameters (mesh, numerical scheme, turbulence model etc.) being identical, the discrepancies observed relative to the slip wall function formulation show that the *implementation* of the wall model alone can lead to significantly different results in a realistic application. Here, the reason for the differences is not necessarily related to the corner problem described in section 3.4. An additional effect could be the tendency of the slip velocity (which forces the near-wall momentum in wall-parallel direction) to keep the flow closely attached to curved geometrical features, which can be expected to delay boundary layer detachment. In this case, the

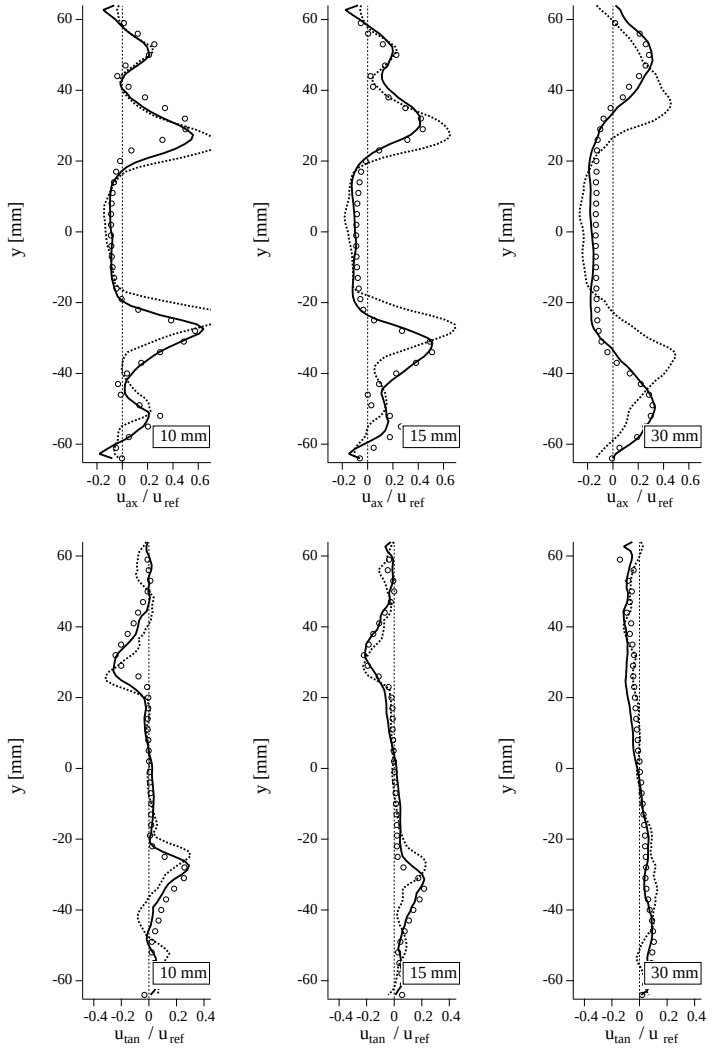

Fig. 23 Mean velocity profiles. Axial component (upper diagram) and tangential component (lower diagram). Comparison of no-slip wall functions (—), slip wall functions (- - -) and experimental data (○ ○ ○).

main flow concentrates along the shape of the inner lip of the injector cone, which results in a more confined shape of the overall flow.

Another important aspect is the numerical robustness of either approach. An instructive way of looking at this issue is to observe the temporal evolution of pressure and slip velocity at a set of probes located on the wall of a narrow channel. The arrangement of the three probes considered is shown in figure 25. The evolution of the slip velocity x-component, presented in figure 26 reveals its very unstable behavior. While it is observed in the turbulent channel flow that the slip-velocity accommodates to the natural near-wall fluctuations to a certain extent (see fig. 14), it becomes clear that in

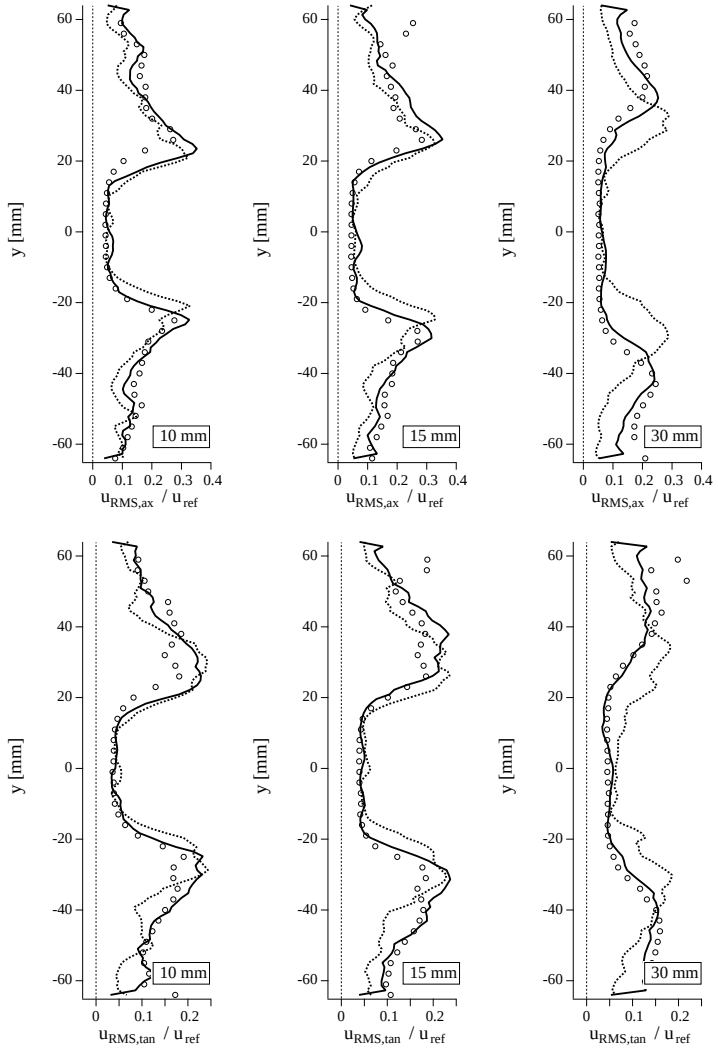

Fig. 24 Velocity fluctuation profiles. Axial component (upper diagram) and tangential component (lower diagram). Comparison of no-slip wall functions (—), slip wall functions (- - -) and experimental data (○ ○ ○).

the case of a less resolved and less regular mesh, the slip-velocity reveals a non-physical strong oscillatory tendency up to the point of briefly taking counterstreamwise orientations. The resulting pressure fluctuations are five times stronger than in the case of the no-slip formulation, as shown in figure 27. Obviously, this would become an issue if the LES was used for aeroacoustics simulations, where wall functions in slip-formulation create a non-physical noise. Furthermore, the advantages of the no-slip formulation in terms of a problem-free (i.e. more robust at locations that are prone to destabilizing the numerics) application by the end-user and the gained rapidity in setting up a simulation should not be under-estimated.

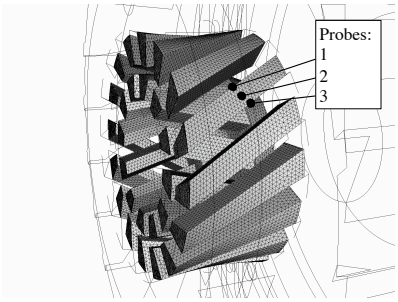

Fig. 25 Location of the pressure probes. View of the two innermost swirler stages.

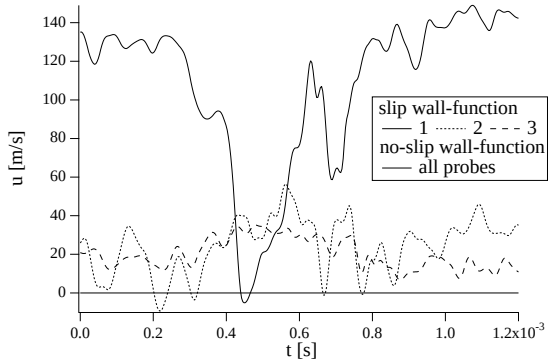

Fig. 26 x-component of the velocity recorded at the three probes over a period of 1.2 milliseconds. Comparison of results from slip- and no-slip wall functions.

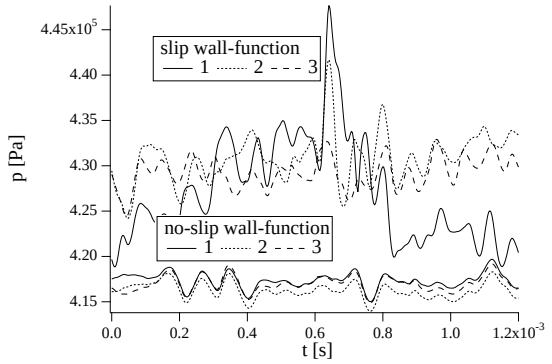

Fig. 27 Pressure signal recorded at the three probes over a period of 1.2 milliseconds. Comparison of results from slip- and no-slip wall functions.

5 Conclusion

Two different implementation methods of wall functions in cell-vertex type solvers have been presented in detail. The classical method imposes the shear-stress from the wall

model directly at the boundary, which results in a slip-velocity at the wall itself. The artificial nature of this slip-velocity and its negative consequences on certain configurations encountered in real-world LES applications has been highlighted. To avoid these difficulties, a formulation with a no-slip condition at the wall is proposed. The wall shear-stress is applied at the first off-wall node, which leads to the necessity of using hexahedral or prismatic meshes in near-wall regions.
Both formulations are compared in different applications. The first is the turbulent, periodic channel flow, which corresponds to a standard validation case and demonstrates the basic capability of both approaches to reproduce global quantities such as the wall-friction coefficient. The second is the flow over a sudden expansion, which illustrates problems that occur at the corner point. As a more realistic application with a complex geometry, an injector for aero-engines is presented.
It is shown that the proposed no-slip formulation has superior qualities in reproducing the experimental velocity profiles, which is explained by the increased tendency of the slip wall functions to force the flow into wall-parallel direction along curved surfaces, resulting in a slightly altered flow topology. Furthermore, the tendency to oscillatory behaviour of the slip-velocity in certain cases and its impact on numerical robustness is highlighted.
It can be stated that in realistic applications, the way a wall-model is implemented in a given code and the way it interacts with the numerical methods used (in particular: scheme and SGS turbulence model) *can* influence the results as much as the wall-model itself. While the present work uses a very basic model, the performance of the proposed no-slip formulation in conjunction with more sophisticated models should be further investigated.

Acknowledgements The authors would like to thank F. Nicoud and G. Puigt for the fruitful discussions on wall-modelig. The authors gratefully acknowledge the support of ONERA Fauga-Mauzac center in providing measurement data as well as the support of F. Jaegle by the European community through a Marie Curie Fellowship (contract MEST-CT-2005-020426).

References

1. Baggett JS, Jimenez J, Kravchenko AG (1997) Resolution requirements in large-eddy simulations of shear flows. Center for Turbulence Research Annual Research Briefs pp 51–66
2. Breuer M, Kniazev B, Abel M (2007) Development of wall models for LES of separated flows using statistical evaluations. Computers & Fluids 36(5):817–837
3. Cabrit O, Nicoud F (2009) Direct simulations for wall modeling of multicomponent reacting compressible turbulent flows. Phys. Fluids 21(055108)
4. Deardorff J (1970) A numerical study of three-dimensional turbulent channel flow at large reynolds numbers. J. Fluid Mech. 41:453–480
5. Dellenback P, Metzger D, Neitzel G (1988) Measurement in turbulent swirling flows through an abrupt axisymmetric expansion. AIAA J. 13(4):669–681
6. Grötzbach (1987) Direct numerical and large eddy simulation of turbulent channel flows. In: Cheremisinoff NP (ed) Encyclopedia of Fluid Mechanics, Gulf, West Orange, NJ, pp 1337–1391

7. Hirsch C (1988) Numerical Computation of internal and external flows. John Wiley, New York
8. Hoffmann G, Benocci C (1995) Approximate wall boundary conditions for large eddy simulations. In: R B (ed) Advances in turbulence V, Kluwer Academic Publishers, pp 222–228
9. Hoyas S, Jiménez J (2006) Scaling of the velocity fluctuations in turbulent channels up to re= 2003. Phys. Fluids 18:011,702
10. Kays W, Crawford M, Weigand B (2004) Convective heat and mass transfer. McGraw-Hill Science/Engineering/Math
11. Knopp T, Alrutz T, Schwamborn D (2006) A grid and flow adaptive wall-function method for RANS turbulence modelling. Journal of Computational Physics 220(1):19–40
12. Mason PJ, Callen NS (1986) On the magnitude of the subgrid-scale eddy coefficient in large-eddy simulations of turbulent channel flow. Journal of Fluid Mechanics Digital Archive 162(-1):439–462
13. Mohammadi B, Puigt G (2006) Wall functions in computational fluid mechanics. Comput. Fluids 35(10):1108–1115
14. Ni RH (1982) A multiple grid scheme for solving the euler equations. AIAA J. 20:1565–1571
15. Nicoud F, Ducros F (1999) Subgrid-scale stress modelling based on the square of the velocity gradient. Flow Turb. and Combustion 62(3):183–200
16. Nicoud F, Baggett J, Moin P, Cabot W (2001) Les wall-modeling based on optimal control theory. Phys. Fluids 13(10):1629–1632
17. Panara D, Porta M, Dannecker R, Noll B (2006) Wall-Functions and Boundary Layer Response to Pulsating and Oscillating Turbulent Channel Flows. In: Proceedings of the 5th International Symposium on Turbulence, Heat and Mass Transfer THMT06
18. Petukhov B (1970) Heat transfer and friction in turbulent pipe flow with variable physical properties. Advances in heat transfer 6:503–564
19. Piomelli U, Balaras E (2002) Wall-layer models for large-eddy simulations. Ann. Rev. Fluid Mech. 34(1):349–374
20. Piomelli U, Ferziger J, Moin P, Kim J (1989) New approximate boundary conditions for large eddy simulations of wall-bounded flows. Physics of Fluids A: Fluid Dynamics 1:1061
21. Piomelli U, Balaras E, Pasinato H, Squires K, Spalart P (2003) The inner–outer layer interface in large-eddy simulations with wall-layer models. Int. J. Heat Fluid Flow 24(4):538–550
22. Poinsot T, Lele S (1992) Boundary conditions for direct simulations of compressible viscous flows. J. Comput. Phys. 101(1):104–129
23. Prandtl L (1925) Bericht über untersuchungen zur ausgebildeten turbulenz. Zeitschrift fur angewandte Mathematik und Mechanik 5:136–139
24. Schmitt P, Poinsot T, Schuermans B, Geigle K (2007) Large-eddy simulation and experimental study of heat transfer, nitric oxide emissions and combustion instability in a swirled turbulent high pressure burner. J. Fluid Mech. 570:17–46
25. Schumann U (1975) Subgrid scale model for finite difference simulations of turbulent flows in plane channels and annuli. J. Comput. Phys. 18:376–404
26. Smagorinsky J (1963) General circulation experiments with the primitive equations: 1. the basic experiment. Monthly Weather Review 91:99–164
27. Spalart P (2009) Detached-eddy simulation. Ann. Rev. Fluid Mech. 41:181–202

28. Spalart P, Jou W, Strelets M, Allmaras S (1997) Comments on the feasibility of LES for wings, and on a hybrid RANS/LES approach. Advances in DNS/LES 1
29. Struijs R (1994) Multi-dimensional upwind discretization method for the Euler equations on unstructured grids. Ph D Thesis Technische Univ, Delft (Netherlands)
30. Tannehill J, Anderson D, Pletcher R (1997) Computational fluid mechanics and heat transfer. Hemisphere Publishing Corporation
31. von Kármán T (1930) Mechanische aehnlichkeit und turbulenz. Nach Ges Wiss Göttingen, Math Phys Klasse 1:58–76